Atmospheric moisture channels and pre-existing weather regimes for rain belt events during East Asian summer monsoon season

Tat Fan Cheng[1], Lun Dai[1] and Mengqian Lu[1, 2]

1 Department of Civil and Environmental Engineering, The Hong Kong University of Science and Technology, Clear Water Bay, Hong Kong, China.

2 Guangzhou HKUST Fok Ying Tung Research Institute, Nansha, Guangzhou, China.

Corresponding author: Mengqian Lu (mengqian.lu@ust.hk)

Key Points:

- Four main moisture supply corridors from the Somali Jet, South Asia, Bay of Bengal and the Pacific Ocean are identified.
- Pre-existing circulations include the subtropical high, a South Asian Low, a dual-anticyclone pattern and tropical cyclones.
- Three circumglobal Rossby wave trains affect the lower-level circulations and several moisture channels for rain belt events.

Abstract

This study aims to advance the understanding of the pre-existing weather regimes up to two weeks ahead of rain belt events during the East Asian summer monsoon season. To this end, we backtrack the moisture trajectories for the rain belt events and classify up to 15 clusters of rain belt events using curve clustering. The clustered moisture channels reveal four main corridors from the Somali Jet, South Asia, Bay of Bengal and the Pacific Ocean, which are associated with different rain belt event characteristics and moisture sources. Pre-existing weather regimes, such as the zonal oscillation of the western North Pacific subtropical high, a South Asian Low, a dual-anticyclone pattern, tropical cyclones and circumglobal wave trains, are attributable to the preconditioning for rain belt events. Findings from this work may offer insights into the sources of predictability, model evaluation and short-term prediction on rain belt events in East Asia.

Keywords: East Asian summer monsoon, rain belt events, moisture trajectories and corridors, sources of predictability

Plain Language Summary

Strong rain belts in the summer monsoon season are known to cause devastating hazards to both the natural ecosystem and human society. Despite a rapid evolution in computing power and a fuller knowledge of atmospheric sciences, it is still challenging for numerical models to skillfully forecast precipitation at a lead time greater than five days. Apart from the resolution limits and unresolvable chaos and numerical errors, the interaction between the large-scale environments and precipitation is also essential but remains poorly understood. Hence, we aim to advance the understanding of the pre-existing weather regimes up to two weeks ahead of rain belt events during the East Asian summer monsoon season. The work begins from backtracking the moisture trajectories for individual rain belts, in which 15 moisture channels along mainly four moisture corridors are identified. These channels are associated with different rain belt events characteristics and moisture sources. Prominent weather regimes that are responsible for steering the moisture channels are identified and discussed with literature. Findings from this work may offer insights into numerical simulation evaluation, the sources of predictability and short-term prediction on rain belt events in East Asia.

1 Introduction

The east-west elongated rain belts are the most influential and iconic phenomenon during the East Asian summer monsoon (EASM) season, often spawn damaging floods and landslides. And its northward propagation on the intraseasonal time scale orchestrates distinct monsoon stages in various parts of East Asia, such as the Pre-Meiyu, Meiyu/Baiu and Changma/mid-summer stages (Chiang et al., 2017; Dai et al., 2020a, 2020b; Ding & Chan, 2005; Tao & Chen, 1987).

Although intensive efforts were made to study the immediate causes of the rain belt formation and distributions (Li et al., 2018; Tomita et al., 2011; Xu et al., 2009), factors on the scale of two weeks, such as moisture sources, water vapor channels and the governing atmospheric circulations, could be equally important for rain belt formation but were often overlooked and poorly understood. Further, despite a rapid evolution in numerical weather prediction (NWP) (Bauer et al., 2015), forecasting precipitation at lead times greater than five days remains challenging (Kang et al., 2011; Shrestha et al., 2013). Apart from the resolution limits, unresolvable chaos and numerical errors, an accurate rainfall forecasting also requires an understanding of the interaction between the synoptic environments and convection (Arakawa, 1993; Richard et al., 2003). Hence, identifying salient weather regimes related to rain belt events could pinpoint the links of circulations across latitudes and atmospheric layers, the sources of predictability and evaluate models' physical representations.

Recently, there has been growing interest in the atmospheric water cycle related to the summer rainfall in East Asia using moisture tracking models (Cheng & Lu, 2020; Fremme & Sodemann, 2019; Lu & Hao, 2017; Wang et al., 2018) and algorithms (Pan & Lu, 2019, 2020). These studies relate local and external water vapor recycling and their associated moisture channels to the intensity and variability of EASM rainfall. We speculate that several pre-existing circulations modulate the moisture supply channels for the downstream heavy rain belts and could be useful for rain belt prediction.

Given the research gap and the challenge in NWP precipitation forecasts, the present study strives to investigate the synoptic weather regimes in a two-week window ahead of the rain belt events in East Asia. To achieve this goal, we backtrack the moisture from rain belts using a moisture tracking model. We then utilize the derived sources' strength for each rain belt to construct the rain belt event catalog. We will show that the backtracked moisture trajectories help unveil the essential water vapor channels and the atmospheric circulations at play.

2 Data and Methods

2.1 Data

Meteorological variables are retrieved from the fifth generation of the European Centre for Medium-Range Weather Forecast (ECMWF) atmospheric reanalysis data (ERA5) between 1981 and 2018 at 1° grid resolution for diagnoses (Copernicus Climate Change Service, 2017). ERA5 data at 0.25°×0.25° grid resolution is adopted as the input for the moisture tracking model. Best track data from the Hong Kong Observatory in the International Best Track Archive for Climate Stewardship (IBTrACS) are adopted for tracking tropical cyclones (Knapp et al., 2010, 2018).

2.2 Moisture tracking model

We use the dynamical recycling model (DRM) (Dominguez et al., 2006; Martinez & Dominguez, 2014) for moisture backtracking. It is a two-dimensional semi-Lagrangian offline moisture tracking model forced by the ERA5 reanalysis data. It has been adopted to derive the relative contributions from local or external sources at a daily level in different monsoon regions with good fidelity and low computational demand (Cheng & Lu, 2020; Hu & Dominguez, 2015; Martinez & Dominguez, 2014; Pathak et al., 2017). The recycling ratio R in the DRM represents the fraction of precipitation in a sink grid recycled from a source's evapotranspiration along the backward trajectory. It can be computed analytically with a semi-Lagrangian scheme (Dominguez et al., 2006):

$$R(x,y,t) = 1 - exp\left[-\int_0^{\tau} \frac{E(x',y',t')}{W(x',y',t')} d\tau'\right], \qquad (1)$$

where E is evapotranspiration, W is precipitable water in the semi-Lagrangian coordinate (x', y', t'). This equation can be further written as the sum of the relative contribution terms from each source along the trajectory (Martinez & Dominguez, 2014). Following Cheng & Lu (2020)'s work, we prescribe 30 source regions within a model domain of 20°S-65°N, 30°-190°E to construct the source-receptor network for each rain belts (Fig. S1). The backward tracking algorithm is performed at a 10-min time interval, and it stops once the tracking time exceeds 14 days, or the trajectory reaches the domain boundaries.

2.3 EASM rain belt events detection

Daily rain belts are detected within 15°-45°N, 105°-145°E from April through September in 1981-2018 by the following criteria. First, the rainfall amount at each 1° grid needs to be greater than its local threshold, which is the smoothed 80th percentile of the wet day precipitation (>1 mm day^{-1}) by the Gaussian kernel smoothing. By connecting the heavy rainfall grids from eight directions with no gaps allowed, a rain belt is detected if its zonal extent is greater than 10° in longitude.

Instead of using spatial overlap to determine a rain belt event, we utilize the DRM-derived recycling ratios to cluster rain belts of similar source origins. For any pair of rain belts occurring on consecutive days, they are deemed the same event if the Euclidean distance D in the recycling ratios of their source-receptor networks is less than 10%. Namely,

$$D(\boldsymbol{R_i}, \boldsymbol{R_j}) = \sqrt{\sum_{l=1}^{n30}[\boldsymbol{R_i}(l) - \boldsymbol{R_j}(l)]^2}, \quad (2)$$

where $\boldsymbol{R_i}$ and $\boldsymbol{R_j}$ are arrays containing the recycling ratios of the 30 sources (Fig. S1) for the pair of rain belts. The 10% threshold in D is chosen as it refers to the level after the peak in the distribution of D from all pairs of rain belts occurring on consecutive days (Fig. S2). All individual rain belts are assigned to an event with the smallest D (i.e., having the most similar source-receptor network) such that each rain belt belongs to one event only.

Finally, 1265 high-impact rain belt events are obtained for analysis, each having at least one rain belt with over 90% of its portion laying within a nested monsoon domain of 20°-40°N, 110°-140°E (Ding & Chan, 2005). Examples of the detected events are given in Fig. S3 for readers' reference.

2.4 Trajectories clustering

Based on our preliminary analysis, the East Asian rain belt events are supplied by several moisture supply channels (e.g., Figs. S3b, d). As such, we classify the DRM-derived moisture trajectories of the first rain belt affecting the EASM domain in all 1265 events using an Expectation-Maximization (EM)-based curve clustering algorithm (Gaffney, 2004). A 4th order polynomial regression model is trained in the curve clustering. The optimal number of clusters is 15, where the trained likelihood plateaus (Fig. S4). Readers may find examples of events with the clustered moisture trajectories in Fig. S5.

Finally, we assign a rain belt event to the cluster if over 30% of the first rain belt's back trajectories affecting the EASM domain belong to that cluster, leaving only 7% of the events without any membership, 21% with two or more cluster memberships.

2.5 Rossby wave source and wave activity flux

In the weather diagnosis, we compute the Rossby wave source S (s^{-2}) using Sardeshmukh & Hoskins (1988)'s definition:

$$S = -\eta D - v_\chi \cdot \nabla\eta, \tag{3}$$

where v_χ is the divergent wind (m s^{-1}), η is the absolute vorticity (s^{-1}) and D is the divergence of wind (s^{-1}). Hence, S is contributed by the rate of change of vorticity due to vortex stretching and the vorticity advection by v_χ.

We are also interested in the wave activity flux W (m^2 s^{-2}) for stationary Rossby wave on a pressure level (Takaya & Nakamura, 2001), which can be written as

$$W = \frac{1}{2|\overline{U}|}\begin{bmatrix} \bar{u}\left({\psi'_x}^2 - \psi'\psi'_{xx}\right) + \bar{v}(\psi'_x\psi'_y - \psi'\psi'_{xy}) \\ \bar{u}(\psi'_x\psi'_y - \psi'\psi'_{xy}) + \bar{v}({\psi'_y}^2 - \psi'\psi'_{yy}) \end{bmatrix}, \tag{4}$$

where $\overline{U} = (\bar{u}, \bar{v})$ is the climatological wind velocities (m s^{-1}) and ψ' is the perturbation stream function (m^2 s^{-1}) from the climatological state. The subscript denotes partial derivative. Both the Rossby wave source and the wave activity fluxes are computed on spectral harmonics. We select the 200-hPa pressure level for investigation as wave sources generally peak at this level (Scaife et al., 2017).

3 Results

3.1 Main moisture corridors for EASM rain belt events

By clustering the DRM backtrack trajectories (Section 2.4), the resultant 15 clusters (hereafter denoted as C1 to C15) unveil four main corridors of moisture transport for East Asian rain belt events (Fig. 1a). They are the Somali corridor (C1 and C12), the Bay of Bengal corridor (C5, C10 and C15), South Asian corridor (C3, C7, C8 and C9) and the Pacific corridor (C6, C11 and C13). By attributing 63.7%-75.4% of the precipitation in rain belt events to the upwind sources in the past two weeks using the DRM (Fig. 1b), each moisture corridor is uniquely supplied by different sets of dominant sources. For instance, rain belt events in C5, C10 and C15 from the Bay of Bengal corridor receive substantial amounts of moisture from the Bay of Bengal (9%-21.7%) and the Indochina (~10%) (Fig. 1b). Likewise, the Philippine Sea that lies beneath the Pacific corridor supplies over 20% of the rain belts in C6, C11 and C13. It is noteworthy that the South Asian corridor (C3, C7, C8 and C9) takes up moisture mostly from terrestrial sources, such as the Indian subcontinent, Southwest China and Indochina. Further, seven out of the 15 clusters heavily rely on moisture from land sources (Fig. S6). These results underscore the importance of the upwind terrestrial sources in the downwind rain belt events during the EASM season (Cheng & Lu, 2020; Keys et al., 2014; Wang-Erlandsson et al., 2018).

Apart from the source-receptor networks and the tracked moisture pathways, the rain belt events themselves also reveal different characteristics across clusters. Statistically, the rain belt events fed by a long-range moisture channel over oceans (e.g., C1, C12, C13 and C15) are slightly more persistent (Fig. 1c) and bring more rainfall to the EASM domain (Fig. 1d). This finding suggests that strong and persistent rainfall events tend to be sustained by strong moisture transport from remote oceanic sources, which has been found the case for various extratropical regions (Lavers et al., 2011; Lu et al., 2013; Lu & Hao, 2017; Pan & Lu, 2019). In contrast, moisture channels from mid-latitudes (C2), the South China Sea (C14) and foothills of the Himalayas (C3) are more associated with weaker and shorter rain belt events in East Asia (Figs. 1c, d).

Interestingly, the arrival timings of the spatially clustered rain belt events also synchronize. Events fed by the South Asian corridor (C3, C7, C8 and C9) have their arrival timings peak in April to mid-May (Fig. 1e), which corresponds to the Spring and Pre-Meiyu stages in East Asia (Dai et al., 2020a). While, strong and persistent rain belt events fed by the moisture from the Somali corridor (C1 and C12) mainly occur in mid-June to early July (i.e., Meiyu stage) when the Somali jets, Indian summer monsoon and the EASM are all the strongest (Chang & Chen, 1995; Dai et al., 2020a). Events in C6 and C13 of the Pacific corridor, in contrast, tend to occur during the peak typhoon season (i.e., late summer).

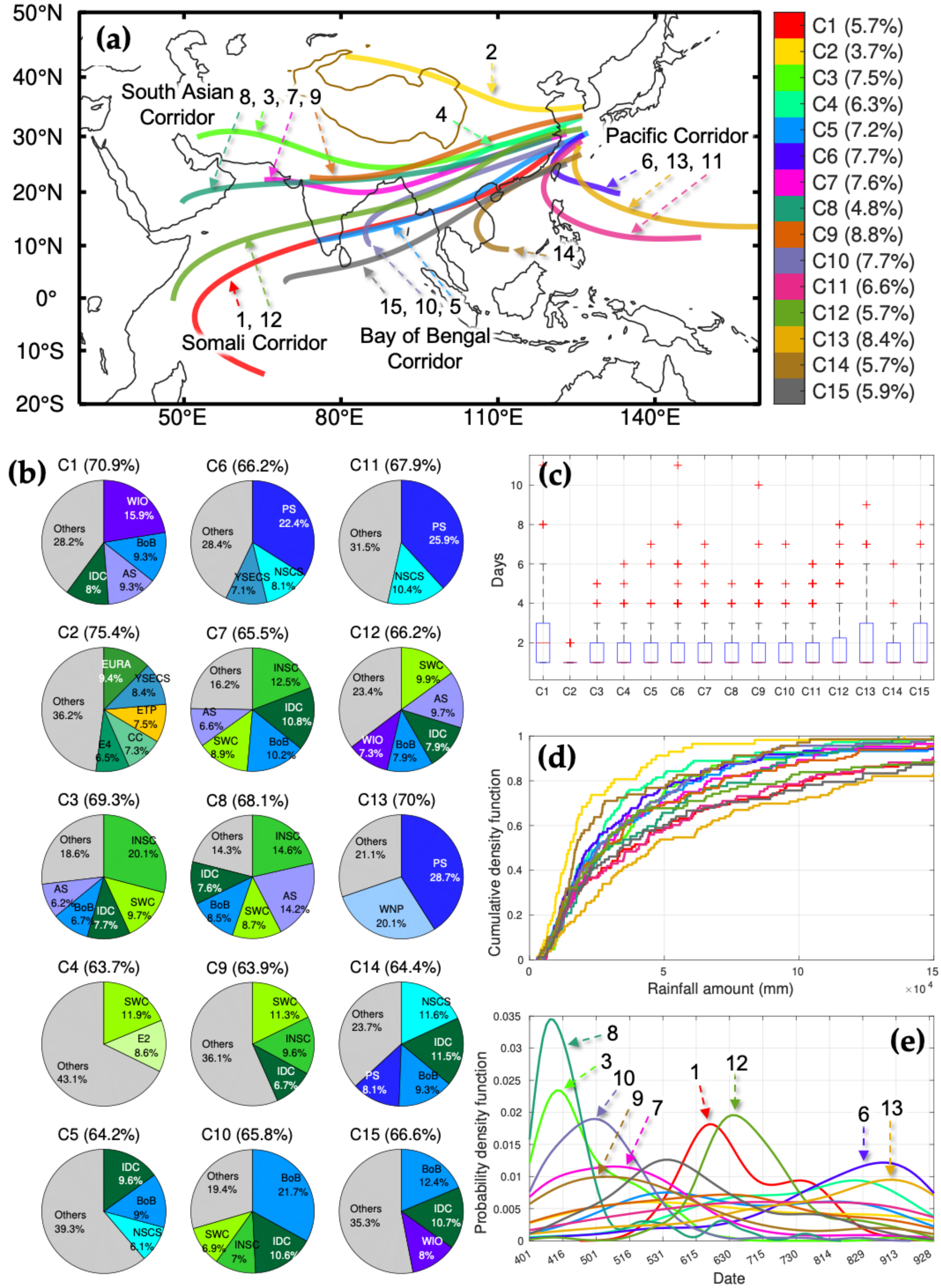

Fig. 1. (a) 15 regression curve clusters (hereafter denoted as C1 to C15) from the backward moisture trajectories of East Asian rain belt events from April to September in 1981-2018. The parentheses in the color bar show the percentages of

the total number of trajectories (~one million) assigned to individual clusters. **(b)** Pie charts of source contributions to rain belt events of each cluster. Only the top three sources are labeled with the acronyms and the relevant recycling ratios. The definition of acronyms can be found in the caption of Fig. S1. Single source contribution less than 6% is grouped into the category "Others." The total attributed fractions of precipitation are shown in the subtitles of each pie chart. **(c)** Box plots of event durations in each cluster. **(d)** The cumulative density function of the total rainfall amount precipitated in the monsoon domain (i.e., 20˚-40˚N, 110˚-140˚E) for each cluster. **(e)** The probability density function of the arrival timing of rain belt events in each cluster. Line colors in (d) and (e) correspond to the same colorings as in (a).

3.2 Governing atmospheric circulations

Given the distinct moisture channels for the East Asian rain belt events, we construct composites of weather maps at different lead times to understand how those water vapor channels are formed in the first place and what are the governing atmospheric circulations. Note that anomaly fields in the composites are the mean deviations of daily fields from the 5-day-moving-mean daily climatology (1981-2018).

3.2.1 South Asian low–western North Pacific subtropical high (SAL-WNPSH) coupling

Regarding the Somali corridor (C1 and C12) (Fig. 1a), their weather composites involve two canonical circulations during the summer monsoon season in Asia –– the South Asian low (SAL) and the western North Pacific subtropical high (WNPSH). The former refers to the abundant monsoonal rainfall in the Indian peninsula, while the latter assists in the frontogenesis in East Asia (Chang et al., 2000; Cheng et al., 2019). From C1's composites, we observe a strong SAL accompanied by anomalously strong Somali jets and westerly IVT over the Indian Ocean from 11 days through 3 days ahead (Fig. 2a). Following the SAL's demise, the WNPSH strengthens and extends westward at 10˚-20˚N on day 0, favoring southwesterly IVT and frontal convergence over the entire EASM domain. Such sequential emergence of the SAL and the WNPSH (hereafter termed as the SAL-WNPSH coupling) opens a moisture highway by connecting the Somali jets, Indian and East Asian southwesterly monsoons. A similar SAL-WNPSH coupling is also found in C12's composites (Fig. 2b).

Although C8 corresponds to the South Asian corridor rather than the Somali one, we observe coupling between a much stronger SAL and a weaker WNPSH (Fig. 2c). In this case, the SAL first emerges in the Middle East on day -11, then rapidly deepens and extends eastward since day -7 and lastly merges with the southward-propagating deep trough from mid-latitudes. In this way, the westerly IVT anomalies from South Asia bridges the southwesterly IVT anomalies associated with the weak WNPSH and forms the moisture channel for rain belts in East Asia on Day 0.

As a side note, we reckon that the observed SAL-WNPSH coupling may not be a coincidence. At the upper levels, anomalous 200-hPa divergent winds originated from the SAL converge over the western North Pacific from day -7 onwards in all three clusters' composites (Figs. S7a-c). Hence, by the upper-level interaction of divergent flows, the former SAL likely contributed to the later development of the coupled WNPSH.

Through the way that the SAL-WNPSH coupling steers long-range moisture channels from the Somali Jet (C1 and C12), the associated rain belts tend to impose hydrological threats to South China, mid-lower reaches of the Yangtze river basin and South Japan (Figs. 2d-e). In particular, the South Asian channel (C8) is related to a relatively higher hydrological risk over South China (Fig. 2f), which could be due to the strong moisture convergence there merged from the SAL and the mid-latitude trough (Fig. 2c).

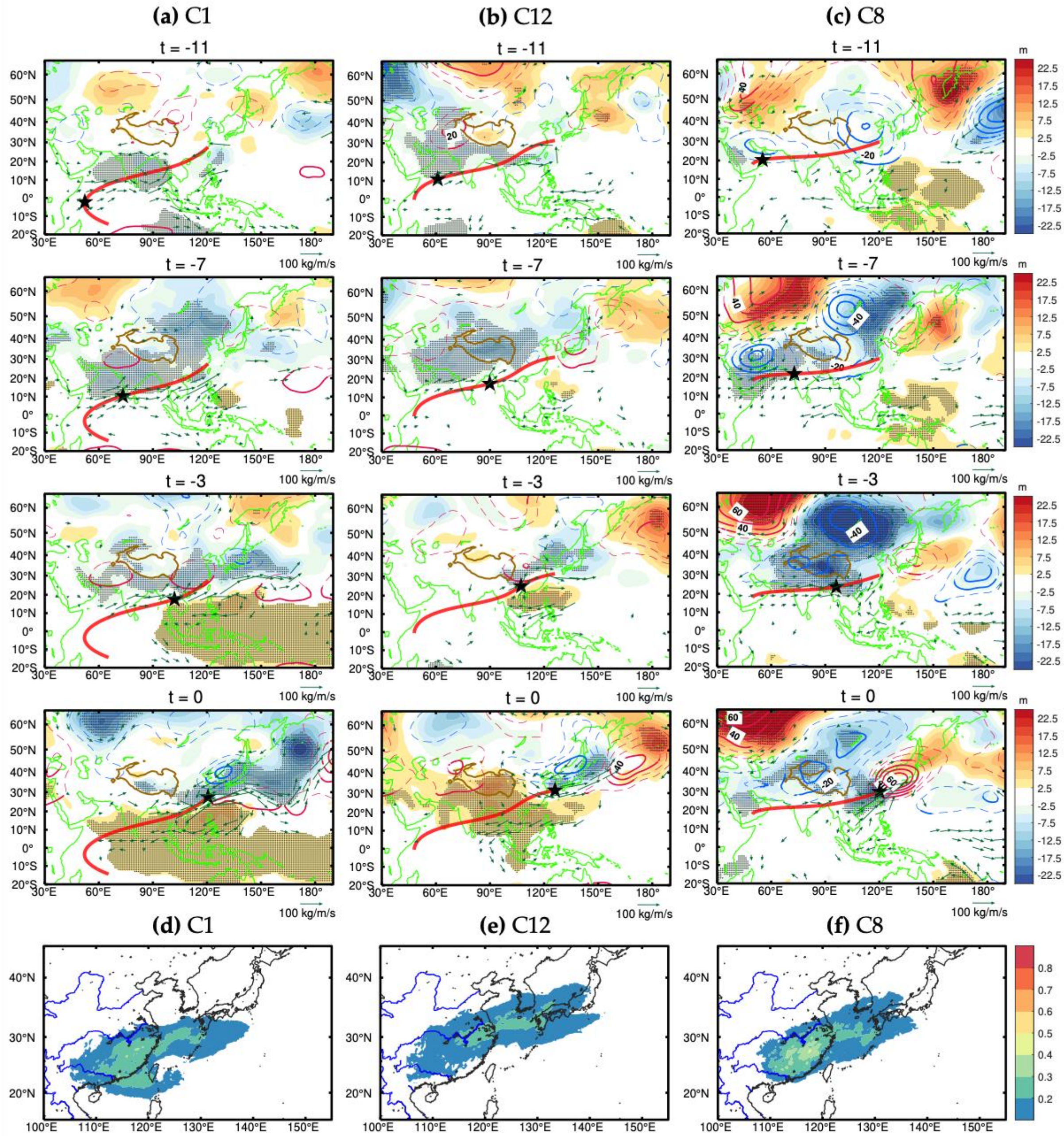

Fig. 2. Composites of 850-hPa geopotential height anomalies (shading, m), 200-hPa geopotential height anomalies (contour, m) and IVT anomalies (vector, kg m^{-1} s^{-1}) at lead times of 11, 7, 3 and 0 days before the occurrence of rain belt events in **(a)** C1 (95 events), **(b)** C12 (93 events) and **(c)** C8 (67 events) and. The solid red line represents the regressed moisture channel for the cluster, along which the black star denotes the regressed position of the moist air column corresponding to the lead time. Contours in red (blue) denote positive (negative) values. Black dots over the shading, thick contours and the shown vectors indicate significant values at the 0.05 level

(Student's *t* test). The last row shows the risk maps of the rain belt occurrence probabilities in **(d)** C1, **(e)** C12 and **(f)** C8.

3.2.2 Dual-anticyclone pattern

Another type of circulation coupling is a dual-anticyclone pattern with an anomalous anticyclone in South Asia followed by the WNPSH, which is often associated with the South Asian moisture corridor (C3, C7 and C9). For instance, from C3's composites, the anticyclonic IVT anomalies over the Indian basin are prominent on day -7 and later accompany a high-pressure anomaly straddling South Asian land (Fig. 3a). The presence of the anomalous anticyclone effectively weakens the westerly moisture transport over the Indian Ocean. Following the anticyclone in South Asia, the WNPSH strengthens and steers southwesterly moisture from day -4 onwards. Similarly, we observe dual anticyclones in the composites of C7 and C9 with slightly different timings and strengths (Figs. 3b, c). The interplay of the two anticyclones blocks much moisture from the Indian Ocean while maintaining the westerly moisture transport over South Asian land, which explains the South Asian corridor and thereby the leading contributions from terrestrial sources for these clusters (Fig. 1b). Consider the hydrological risks, the prominent dual-anticyclone pattern in C3 is associated with Meiyu-like rain belts (Fig. 3d), which tends to occur in April and May (Fig. 1e). A rather weak dual-anticyclone pattern with the WNPSH centered at slightly different latitudes favor localized rain belts in South China (Fig. 3e) and in South Korea and Japan (Fig. 3f).

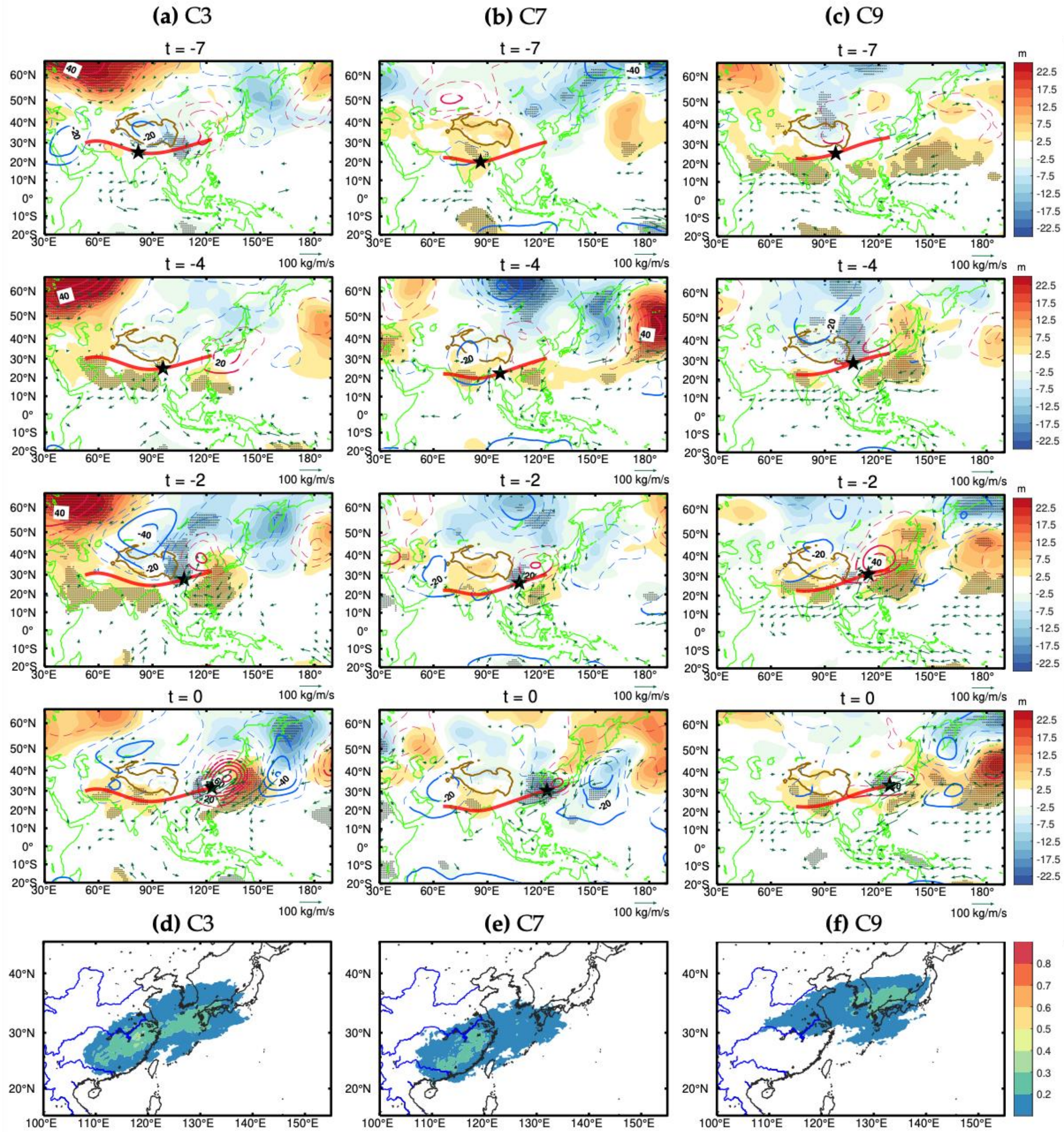

Fig. 3. As in Fig. 2, but for **(a), (d)** C3 (106 events), **(b), (e)** C7 (84 events) and **(c), (f)** C9 (129 events) on day -7, -4, -2 and 0.

3.2.3 Tropical cyclones and the zonal WNPSH oscillation

Clusters of the Pacific corridor (C6, C11 and C13) bear high similarity in their weather composites. An anomalous cyclone emerges over the western Pacific one week before the rain belt events (Figs. S8a-c). As it propagates towards East Asia, the accompanied southeasterly IVT anomalies to its northeast carry abundant moisture from the Pacific Ocean and contribute to intensive rain belt events alongshore and over the Eastern China Sea (Figs. S8d-f). Further statistics using the best track data (Section 2.1) suggests that substantial percentages of rain belt events in C6 (59%), C11 (60%) and C13 (78%) co-occur with tropical cyclones with maximum sustained wind of at least 33 knots. The observational finding confirms the role of tropical cyclones in establishing the Pacific corridor. Additionally, from C6's composites (Fig. S8a), the westward propagation of an anomalous cyclone over the western North Pacific also resembles the scenario when the WNPSH retreats to the east (Cheng et al., 2019).

For clusters of the Bay of Bengal corridor (C5, C10 and C15) and its nearby channels (C4, C14), we observe the westward extension of the WNPSH from day -4 onwards (Figs. S9a-e). Even without any other circulations to couple with, the standalone westward-propagating anticyclone can still draw moisture from the southwest and establish relatively short vapor channels from the Bay of Bengal. As a result, rain belts emerge in various locations, such as South Korea and Japan (Fig. S9f), adjacent oceans (Figs. S9g, h) and South China (Figs. S9i, j), which are in line with the location of the WNPSH's northwest flank where frontogenesis is favored (Cheng et al., 2019).

3.2.4 Circumglobal wave trains

In addition to the lower-level circulations that steer the moisture channels for rain belt events, increasing studies reported the non-trivial role of extratropical Rossby wave trains in East Asian summer rainfall (Cheng & Lu, 2020; Dai et al., 2020b; Stephan et al., 2018). Circumglobal wave patterns were found informative for extreme rainfall events in mid-latitudes (Lu et al., 2013). In this section, we identify three quasi-stationary and circumglobal wave trains (CGTs) with a barotropic structure in two weeks ahead, which acts to modulate the circulations at lower levels that steer the essential moisture channels for the EASM rain belt events.

For C3 that corresponds to an inland moisture channel over South Asia, it is associated with a CGT propagating from the eastern Pacific to the subtropical Atlantic Ocean, northern Africa, Middle East, Tibetan Plateau, East Asia and lastly, back to the Pacific Ocean since day -13 (Fig. 4a). The wave route covering the wide deserts in North Africa and the Middle East makes this CGT different from other known wave trains such as the Silk Road pattern (Enomoto et al., 2003) or the Europe-China pattern (Chen & Huang, 2012). Several anomalous wave sources are found over the central North Pacific, the western North Atlantic, North Africa and the Middle East (Fig. 4b). Subsequently, a strong wave source over India is seen on day -7 (Fig. 4d). In particular, the wave source over North Africa assists in directing the wave train towards the desert regions and leads to an interesting wave pattern. The wave sources over North Africa and the Middle East could be explained by descent motions from the radiative cooling over the arid regions (Enomoto et al., 2003), which causes an upper-level convergence as seen from the negative 200-hPa geopotential height anomalies (Figs. 4b, d). Hence, a vorticity source is induced by the vortex stretching term $-\eta D$ (Eq. 3), whereas the vorticity advection term is negligible (not shown). Taken these features together, we term such a wave phenomenon as the Pacific-Atlantic-Desert-Indian (PADI) pattern.

Such a PADI pattern may induce the lower-level circulation anomalies in South Asia that shape the moisture channel associated with C3. Given its barotropic structure with consistent circulation anomalies at both 200-hPa and 500-hPa levels (Fig. 4a), an anomalous trough to the west of the Tibetan Plateau linked with the wave train helps initiate the inland moisture channel on day -13. As the PADI wave train propagates further east on day -7, an upper-level anticyclone begins to develop over South Asia (Fig. 4c), favoring a high-pressure anomaly at lower-levels since then and thereby the inland moisture channel (Fig. 3a).

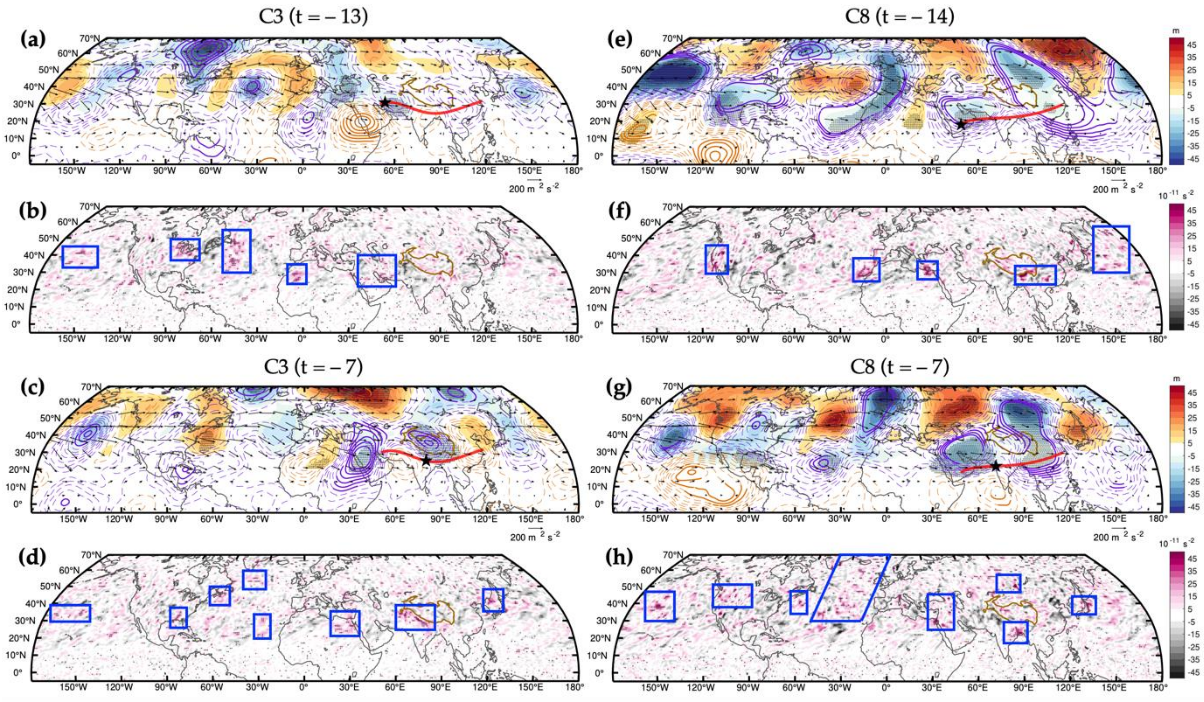

Fig. 4. Composites of **(a)** the wave activity fluxes (vector, $m^2\ s^{-2}$), anomalous 500-hPa geopotential height (shading, m) and the 200-hPa perturbation streamfunction (contour, interval: $4\times10^5\ m^2\ s^{-1}$) and **(b)** anomalous S (shading, $10^{-11}\ s^{-2}$) on day -13 before the occurrence of rain belt events in C3 (106 events). As for (a) and (b), panels **(c)** and **(d)** are for C3 on day -7; **(e)** and **(f)** are for C8 on day -14; **(g)** and **(h)** are for C8 on day -7. In panels (a), (c), (e) and (g), contours in orange (purple) denote positive (negative) values, the solid red line represents the regressed moisture channel for the cluster, and the black star denotes the position of the moist air column along the regressed channel. Blue boxes in panels (b), (d), (f) and (h) indicate the main wave sources. Black dots over the shading and thick contours denote significant values at the 0.05 level (Student's t test).

Interestingly, rain belt events in C8 (supplied by a moisture channel along the South Asian corridor) are associated with two CGTs at different lead times. On day -14 (Fig. 4e), we observe a similar PADI wave train with wave sources found over the Rocky Mountains, eastern tropical Atlantic, the Mediterranean Sea and the nearby deserts (Fig. 4f). This barotropic PADI wave consists of a stationary trough anomaly in the Middle East (Fig. 4e), which may favor the SAL's development from day -11 onwards (Fig. 2c). Meanwhile, we identify another CGT propagates at higher latitudes from the central North Pacific to North Atlantic, western Russia, Lake Baikai, the Sea of Japan and lastly, back to the Pacific (Fig. 4e). The wave train becomes more prominent on day -7 (Fig. 4g) excited by a series of wave sources over the central North Pacific, Rocky Mountains, North Atlantic and central Russia (Fig. 4h). Notably, this CGT considerably resembles one type of the Russia-China (RC) pattern, especially the path segment from western Russia to the north of the Tibetan Plateau and East Asia (see the middle panel of Fig. 9 in Dai et al., 2020b). Taken together, we recognize it as the CGT-RC wave pattern. Recalling the pre-existing weather conditions related to C8 (Fig. 2c), it is likely that the barotropic CGT-RC wave train found two weeks ago carries the deep trough from the Lake Baikai to the south and induce a favorable condition for rain belts formation in East Asia (Figs. 4e, g). We also find a similar CGT-RC pattern with a reversed sign in C2's composites, which gives rise to an anomalous trough over the Sea of Japan at least one week ahead (Fig. S10a). The trough then steers the mid-latitude moisture channel for rain belt events in C2 (Figs. S10b, c).

The last Rossby wave train is referred to as the CGT-Silk Road pattern found two weeks ahead of the rain belt events in C12 that are fed by the Somali corridor. This wave train exhibits a transverse path (Fig. S11a) due to a series of localized wave sources located around 40°N (Figs. S11b, d). The wave train segment covering the Mediterranean Sea, the Caspian Sea and the western Tibetan Plateau reminds us of the well-known Silk Road pattern (Chen & Huang, 2012; Enomoto et al., 2003). Particularly, the CGT-Silk Road pattern triggers an upper-level divergence in South Asia from day -14 to -11 (Figs. S11a, c), which may subsequently favor the rising motion and the SAL from day -11 onwards (Fig. 2b), and eventually, the long-range moisture transport along the Somali corridor.

4 Conclusions

This study aims to unveil a fuller picture of the moisture supply channels and pre-existing weather regimes in two weeks ahead of the East Asian rain belt events from the atmospheric water cycle's perspective. By clustering the backtracked moisture trajectories from the rain belt events, we show 15 event clusters with distinct moisture channels along four main corridors, each from the Somali Jet, South Asia, Bay of Bengal and the Pacific Ocean. Seven out of the 15 clusters heavily rely on terrestrial moisture sources, especially those fed by the South Asian moisture corridor. Further, strong and persistent rain belt events are found associated with long-range moisture channels over oceans. Regarding the arrival timing, clusters supplied by the South Asian, Somali and Pacific moisture corridors tend to occur in the Spring and Pre-Meiyu stage, the Meiyu/Baiu stage and typhoon season (i.e., late summer), respectively.

We identify several pre-existing weather regimes that steer the distinct moisture channels for the East Asian rain belt events. Specifically, the SAL-WNPSH coupling governs long-range moisture channels, especially those from the Somali corridor. The associated rain belt events impose threats to South China, mid-lower reaches of the Yangtze river basin and South Japan. The proposed PADI pattern and the CGT-Silk Road pattern may favor the SAL's development from the wave train analysis. Further, the upper-level divergent winds originated from the SAL also contribute to the later development of the WNPSH and explains the coupling. In contrast, the dual-anticyclone pattern encompassing South Asia and the western North Pacific governs the channels in the South Asian corridor. Other moisture channels are mostly modulated by rather standalone systems, including the zonal WNPSH oscillation and tropical cyclones. Lastly, the proposed CGT-RC wave pattern in mid-latitudes is attributable to the mid-latitude moisture channel and rain belt formation related to a South Asian moisture channel. These pre-existing weather regimes may offer insights to the sources of predictability, evaluation of model simulation and short-term prediction on the EASM rain belt events.

Acknowledgments

This research contributes to, and is financially supported by the Hong Kong Research Grants Council funded projects (nos. 16201218 & 16200920). The authors appreciate Prof. Francina Dominguez and Dr. Huancui Hu offering the source code for the DRM, which can be accessed by

https://github.com/huancui/DRM_2LDRM. The meteorological data is retrieved from the ERA5 by the European Center for Medium-Range Weather Forecast (ECMWF) at https://www.ecmwf.int/en/forecasts/datasets/reanalysis-datasets/era5. The IBTrACS best track data can be accessed from https://www.ncdc.noaa.gov/ibtracs/index.php?name=ib-v4-access. Some figures in this paper are generated using a Matlab package "M_Map" (Pawlowicz, 2020).

References

Arakawa, A. (1993). Closure Assumptions in the Cumulus Parameterization Problem. In *The Representation of Cumulus Convection in Numerical Models* (pp. 1–15). American Meteorological Society. https://doi.org/10.1007/978-1-935704-13-3_1

Bauer, P., Thorpe, A., & Brunet, G. (2015). The quiet revolution of numerical weather prediction. *Nature*, *525*(7567), 47–55. https://doi.org/10.1038/nature14956

Chang, C.-P., & Chen, G. T. J. (1995). Tropical Circulations Associated with Southwest Monsoon Onset and Westerly Surges over the South China Sea. *Monthly Weather Review*, *123*(11), 3254–3267. https://doi.org/10.1175/1520-0493(1995)123<3254:tcawsm>2.0.co;2

Chang, C.-P., Zhang, Y., & Li, T. (2000). Interannual and Interdecadal Variations of the East Asian Summer Monsoon and Tropical Pacific SSTs. Part I: Roles of the Subtropical Ridge. *Journal of Climate*, *13*(24), 4310–4325. https://doi.org/10.1175/1520-0442(2000)013<4310:IAIVOT>2.0.CO;2

Chen, G., & Huang, R. (2012). Excitation mechanisms of the teleconnection patterns affecting the July precipitation in Northwest China. *Journal of Climate*, *25*(22), 7834–7851. https://doi.org/10.1175/JCLI-D-11-00684.1

Cheng, T. F., & Lu, M. (2020). Moisture source-receptor network of the East Asian summer monsoon land regions and the associated atmospheric steerings. *Journal of Climate*, 1–1. https://doi.org/10.1175/JCLI-D-19-0868.1

Cheng, T. F., Lu, M., & Dai, L. (2019). The zonal oscillation and the driving mechanisms of the extreme western North Pacific subtropical high and its impacts on East Asian summer precipitation. *Journal of Climate*, *32*(10), 3025–

3050. https://doi.org/10.1175/JCLI-D-18-0076.1

Chiang, J. C. H., Swenson, L. M., & Kong, W. (2017). Role of seasonal transitions and the westerlies in the interannual variability of the East Asian summer monsoon precipitation. *Geophysical Research Letters*, *44*(8), 3788–3795. https://doi.org/10.1002/2017GL072739

Copernicus Climate Change Service. (2017). *ERA5: Fifth generation of ECMWF atmospheric reanalyses of the global climate*. Copernicus Climate Change Service Climate Data Store (CDS). https://cds.climate.copernicus.eu/cdsapp#!/dataset/reanalysis-era5-single-levels?tab=overview

Dai, L., Cheng, T. F., & Lu, M. (2020a). A neural-network-based approach to define East Asian monsoon annual cycle. *Geophysical Research Letters*, (Submiitted).

Dai, L., Cheng, T. F., & Lu, M. (2020b). Summer Monsoon Rainfall Patterns and Predictability over Southeast China. *Water Resources Research*, *56*(2), 1–21. https://doi.org/10.1029/2019WR025515

Ding, Y., & Chan, J. C. L. (2005). The East Asian summer monsoon: An overview. *Meteorology and Atmospheric Physics*, *89*(1–4), 117–142. https://doi.org/10.1007/s00703-005-0125-z

Dominguez, F., Kumar, P., Liang, X.-Z. Z., & Ting, M. (2006). Impact of atmospheric moisture storage on precipitation recycling. *Journal of Climate*, *19*(8), 1513–1530. https://doi.org/10.1175/JCLI3691.1

Enomoto, T., Hoskins, B. J., & Matsuda, Y. (2003). The formation mechanism of the Bonin high in August. *Quarterly Journal of the Royal Meteorological Society*, *129*(587 PART A), 157–178. https://doi.org/10.1256/qj.01.211

Fremme, A., & Sodemann, H. (2019). The role of land and ocean evaporation on the variability of precipitation in the Yangtze River valley. *Hydrology and Earth System Sciences*, *23*(6), 2525–2540. https://doi.org/10.5194/hess-23-2525-2019

Gaffney, S. J. (2004). *Probabilistic Curve-Aligned Clustering and Prediction with*

Regression Mixture Models. UNIVERSITY OF CALIFORNIA, IRVINE.

Hu, H., & Dominguez, F. (2015). Evaluation of Oceanic and Terrestrial Sources of Moisture for the North American Monsoon Using Numerical Models and Precipitation Stable Isotopes. *Journal of Hydrometeorology*, *16*(1), 19–35. https://doi.org/10.1175/JHM-D-14-0073.1

Kang, S. D., Shin, D. W., Cocke, S., Kim, H. D., & Jung, W. S. (2011). Comparison of ensemble methods for summer-time numerical weather prediction over East Asia. *Meteorology and Atmospheric Physics*, *113*(1), 27–38. https://doi.org/10.1007/s00703-011-0148-6

Keys, P. W., Barnes, E. A., Van Der Ent, R. J., & Gordon, L. J. (2014). Variability of moisture recycling using a precipitationshed framework. *Hydrology and Earth System Sciences*, *18*(10), 3937–3950. https://doi.org/10.5194/hess-18-3937-2014

Knapp, K. R., Diamond, H. J., Kossin, J. P., Kruk, M. C., & Schreck, C. J. I. (2018). *International Best Track Archive for Climate Stewardship (IBTrACS) Project, Version 4. [West Pacific]*. NOAA National Centers for Environmental Information. https://doi.org/https://doi.org/10.25921/82ty-9e16

Knapp, K. R., Kruk, M. C., Levinson, D. H., Diamond, H. J., & Neumann, C. J. (2010). The international best track archive for climate stewardship (IBTrACS). *Bulletin of the American Meteorological Society*, *91*(3), 363–376. https://doi.org/10.1175/2009BAMS2755.1

Lavers, D. a., Allan, R. P., Wood, E. F., Villarini, G., Brayshaw, D. J., & Wade, A. J. (2011). Winter floods in Britain are connected to atmospheric rivers. *Geophysical Research Letters*, *38*(23), L23803. https://doi.org/10.1029/2011GL049783

Li, H., Hu, Y., Zhou, Z., Peng, J., & Xu, X. (2018). Characteristic Features of the Evolution of a Meiyu Frontal Rainstorm with Doppler Radar Data Assimilation. *Advances in Meteorology*, *2018*. https://doi.org/10.1155/2018/9802360

Lu, M., & Hao, X. (2017). Diagnosis of the tropical moisture exports to the mid-latitudes and the role of atmospheric steering in the extreme precipitation. *Atmosphere*, *8*(12). https://doi.org/10.3390/atmos8120256

Lu, M., Lall, U., Schwartz, A., & Kwon, H. (2013). Precipitation predictability associated with tropical moisture exports and circulation patterns for a major flood in France in 1995. *Water Resources Research*, *49*(10), 6381–6392. https://doi.org/10.1002/wrcr.20512

Martinez, J. A., & Dominguez, F. (2014). Sources of Atmospheric Moisture for the La Plata River Basin*. *Journal of Climate*, *27*(17), 6737–6753. https://doi.org/10.1175/JCLI-D-14-00022.1

Pan, M., & Lu, M. (2019). A Novel Atmospheric River Identification Algorithm. *Water Resources Research*. https://doi.org/10.1029/2018wr024407

Pan, M., & Lu, M. (2020). East Asia Atmospheric River catalog: Annual Cycle, Transition Mechanism, and Precipitation. *Geophysical Research Letters*, *47*(15). https://doi.org/10.1029/2020gl089477

Pathak, A., Ghosh, S., Alejandro Martinez, J., Dominguez, F., & Kumar, P. (2017). Role of oceanic and land moisture sources and transport in the seasonal and interannual variability of summer monsoon in India. *Journal of Climate*, *30*(5), 1839–1859. https://doi.org/10.1175/JCLI-D-16-0156.1

Pawlowicz, R. (2020). *M_Map: A Mapping package for Matlab* (version 1.4m). www.eoas.ubc.ca/~rich/map.html

Richard, E., Cosma, S., Benoit, R., Binder, R., Buzzi, A., & Kaufmann, P. (2003). Intercomparison of mesoscale meteorological models for precipitation forecasting. *Hydrology and Earth System Sciences*, *7*(6), 799–811. https://doi.org/10.5194/hess-7-799-2003

Sardeshmukh, P. D., & Hoskins, B. J. (1988). The generation of global rotational flow by steady idealized tropical divergence. *Journal of the Atmospheric Sciences*, *45*(7), 1228–1251. https://doi.org/10.1175/1520-0469(1988)045<1228:TGOGRF>2.0.CO;2

Scaife, A. A., Comer, R. E., Dunstone, N. J., Knight, J. R., Smith, D. M., MacLachlan, C., Martin, N., Peterson, K. A., Rowlands, D., Carroll, E. B., Belcher, S., & Slingo, J. (2017). Tropical rainfall, Rossby waves and regional winter climate predictions.

Quarterly Journal of the Royal Meteorological Society, *143*(702), 1–11. https://doi.org/10.1002/qj.2910

Shrestha, D. L., Robertson, D. E., Wang, Q. J., Pagano, T. C., & Hapuarachchi, H. A. P. (2013). Evaluation of numerical weather prediction model precipitation forecasts for short-term streamflow forecasting purpose. *Hydrology and Earth System Sciences*, *17*(5), 1913–1931. https://doi.org/10.5194/hess-17-1913-2013

Stephan, C. C., Klingaman, N. P., Vidale, P. L., Turner, A. G., Demory, M. E., & Guo, L. (2018). A comprehensive analysis of coherent rainfall patterns in China and potential drivers. Part I: Interannual variability. *Climate Dynamics*, *50*(11–12), 4405–4424. https://doi.org/10.1007/s00382-017-3882-8

Takaya, K., & Nakamura, H. (2001). A formulation of a phase-independent wave-activity flux for stationary and migratory quasigeostrophic eddies on a zonally varying basic flow. *Journal of the Atmospheric Sciences*, *58*(6), 608–627. https://doi.org/10.1175/1520-0469(2001)058<0608:AFOAPI>2.0.CO;2

Tao, S., & Chen, L. (1987). A review of recent research on the East Asian summer monsoon in China. In C.-P. Chang & T. N. Krishnamurti (Eds.), *Monsoon Meteorology* (pp. 60–92). Oxford University Press, New York.

Tomita, T., Yamaura, T., & Hashimoto, T. (2011). Interannual variability of the Baiu season near Japan evaluated from the equivalent potential temperature. *Journal of the Meteorological Society of Japan*, *89*(5), 517–537. https://doi.org/10.2151/jmsj.2011-507

Wang-Erlandsson, L., Fetzer, I., Keys, P. W., Van Der Ent, R. J., Savenije, H. H. G., & Gordon, L. J. (2018). Remote land use impacts on river flows through atmospheric teleconnections. *Hydrology and Earth System Sciences*, *22*(8), 4311–4328. https://doi.org/10.5194/hess-22-4311-2018

Wang, N., Zeng, X. M., Guo, W. D., Chen, C., You, W., Zheng, Y., & Zhu, J. (2018). Quantitative diagnosis of moisture sources and transport pathways for summer precipitation over the mid-lower Yangtze River Basin. *Journal of Hydrology*, *559*, 252–265. https://doi.org/10.1016/j.jhydrol.2018.02.003

Xu, W., Zipser, E. J., & Liu, C. (2009). Rainfall characteristics and convective properties of Mei-Yu precipitation systems over South China, Taiwan, and the South China sea. Part I: TRMM observations. *Monthly Weather Review*, *137*(12), 4261–4275. https://doi.org/10.1175/2009MWR2982.1

Figure 1.

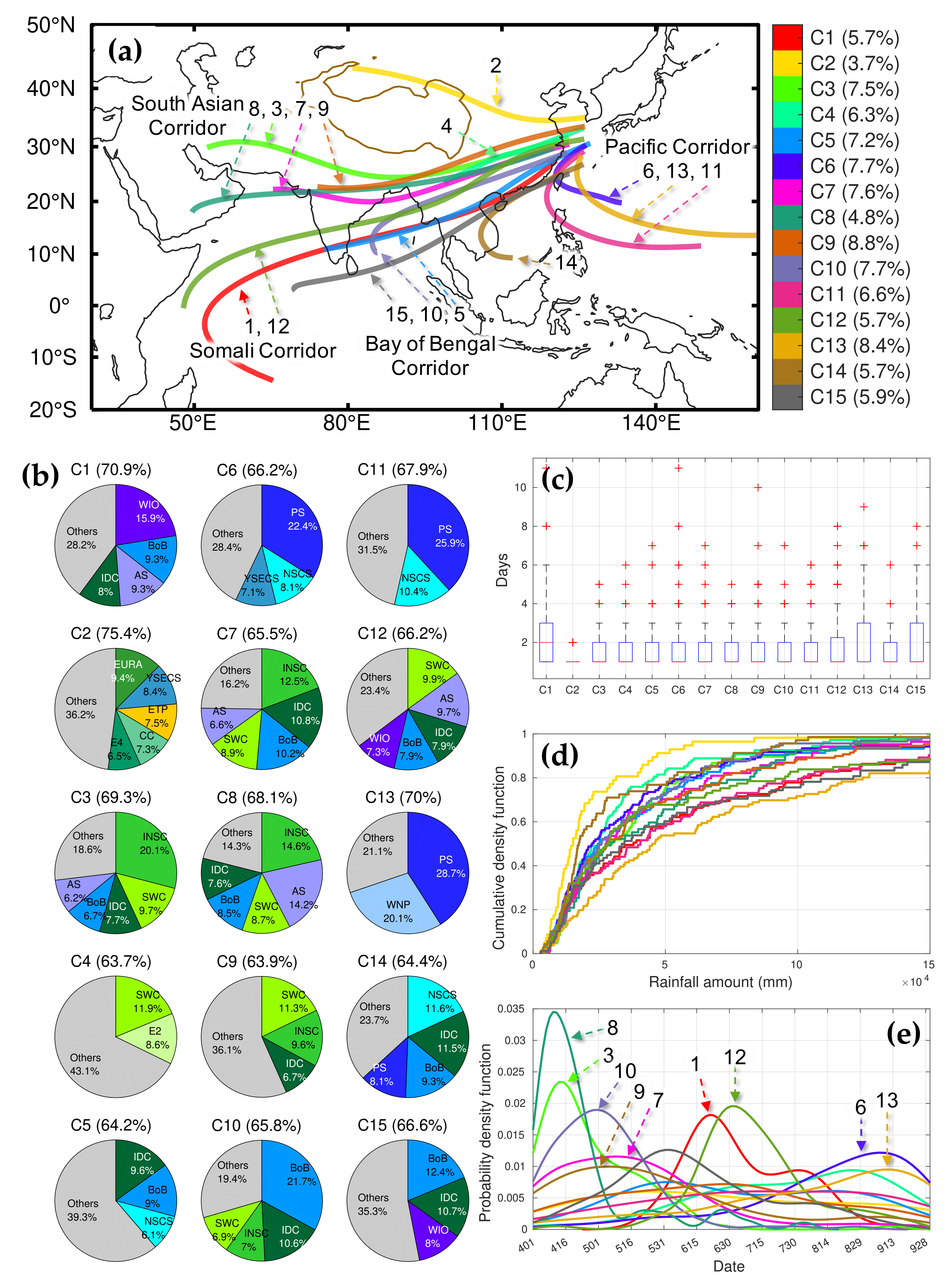
(a)
50°N
40°N
30°N
20°N
10°N
0°
10°S
20°S
50°E
80°E
110°E
140°E
South Asian Corridor
8, 3, 7, 9
2
4
Pacific Corridor
6, 13, 11
14
1, 12
Somali Corridor
15, 10, 5
Bay of Bengal Corridor
C1 (5.7%)
C2 (3.7%)
C3 (7.5%)
C4 (6.3%)
C5 (7.2%)
C6 (7.7%)
C7 (7.6%)
C8 (4.8%)
C9 (8.8%)
C10 (7.7%)
C11 (6.6%)
C12 (5.7%)
C13 (8.4%)
C14 (5.7%)
C15 (5.9%)
(b)
C1 (70.9%)
WIO 15.9%
BoB 9.3%
AS 9.3%
IDC 8%
Others 28.2%
C6 (66.2%)
PS 22.4%
NSCS 8.1%
YSECS 7.1%
Others 28.4%
C11 (67.9%)
PS 25.9%
NSCS 10.4%
Others 31.5%
C2 (75.4%)
EURA 9.4%
YSECS 8.4%
ETP 7.5%
CC 7.3%
E4 6.5%
Others 36.2%
C7 (65.5%)
INSC 12.5%
IDC 10.8%
BoB 10.2%
SWC 8.9%
AS 6.6%
Others 16.2%
C12 (66.2%)
SWC 9.9%
AS 9.7%
IDC 7.9%
BoB 7.9%
WIO 7.3%
Others 23.4%
C3 (69.3%)
INSC 20.1%
SWC 9.7%
IDC 7.7%
BoB 6.7%
AS 6.2%
Others 18.6%
C8 (68.1%)
INSC 14.6%
AS 14.2%
SWC 8.7%
BoB 8.5%
IDC 7.6%
Others 14.3%
C13 (70%)
PS 28.7%
WNP 20.1%
Others 21.1%
C4 (63.7%)
SWC 11.9%
E2 8.6%
Others 43.1%
C9 (63.9%)
SWC 11.3%
INSC 9.6%
IDC 6.7%
Others 36.1%
C14 (64.4%)
NSCS 11.6%
IDC 11.5%
BoB 9.3%
PS 8.1%
Others 23.7%
C5 (64.2%)
IDC 9.6%
BoB 9%
NSCS 6.1%
Others 39.3%
C10 (65.8%)
BoB 21.7%
IDC 10.6%
INSC 7%
SWC 6.9%
Others 19.4%
C15 (66.6%)
BoB 12.4%
IDC 10.7%
WIO 8%
Others 35.3%
(c)
Days
C1 C2 C3 C4 C5 C6 C7 C8 C9 C10 C11 C12 C13 C14 C15
(d)
Cumulative density function
Rainfall amount (mm)
×10^4
(e)
Probability density function
Date
401 416 501 516 531 615 630 715 730 814 829 913 928
8
3
10
9
7
1
12
6
13

Figure 2.

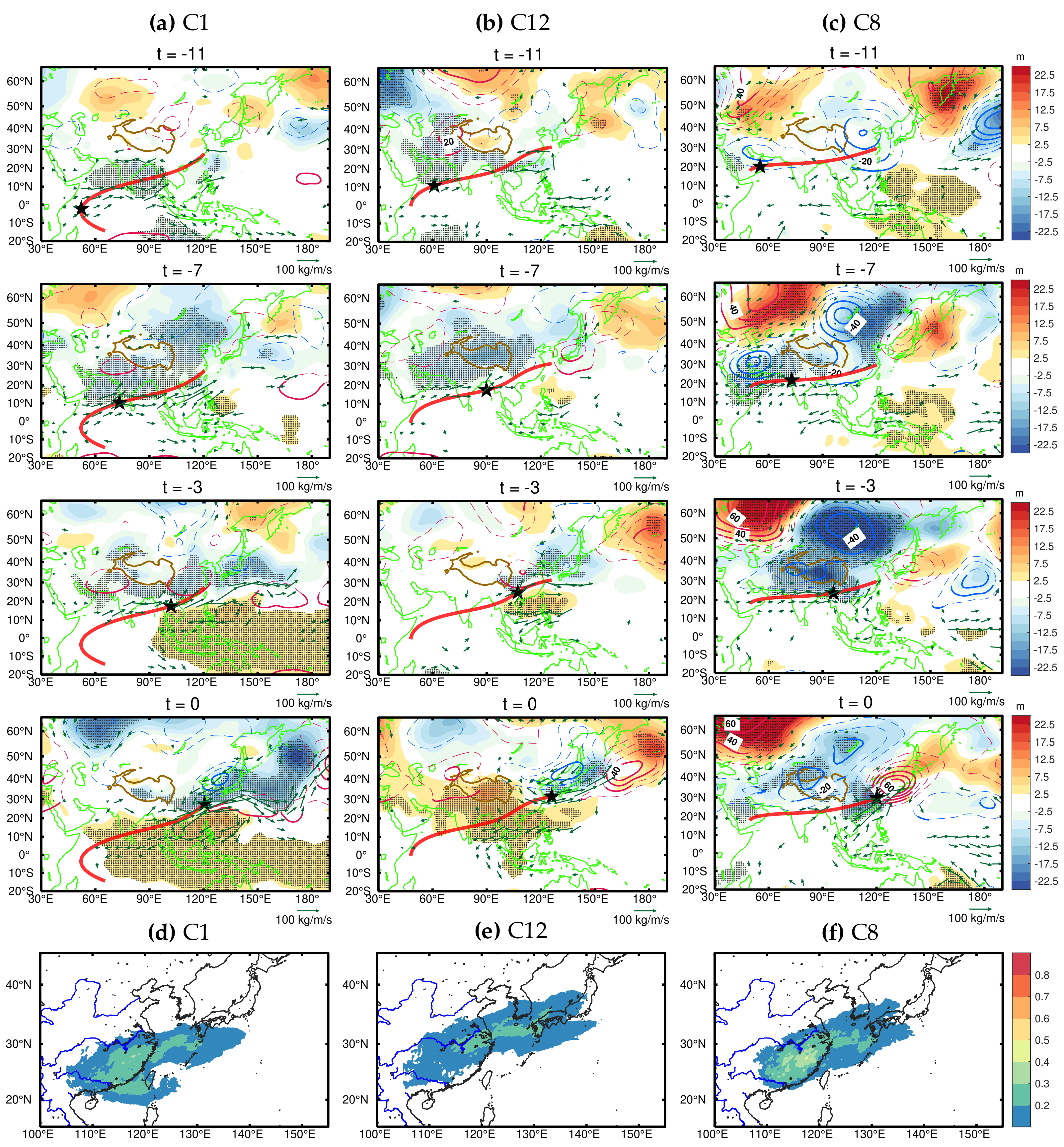
(a) C1
(b) C12
(c) C8
t = -11
t = -7
t = -3
t = 0
100 kg/m/s
m
22.5
17.5
12.5
7.5
2.5
-2.5
-7.5
-12.5
-17.5
-22.5
(d) C1
(e) C12
(f) C8
0.8
0.7
0.6
0.5
0.4
0.3
0.2

Figure 3.

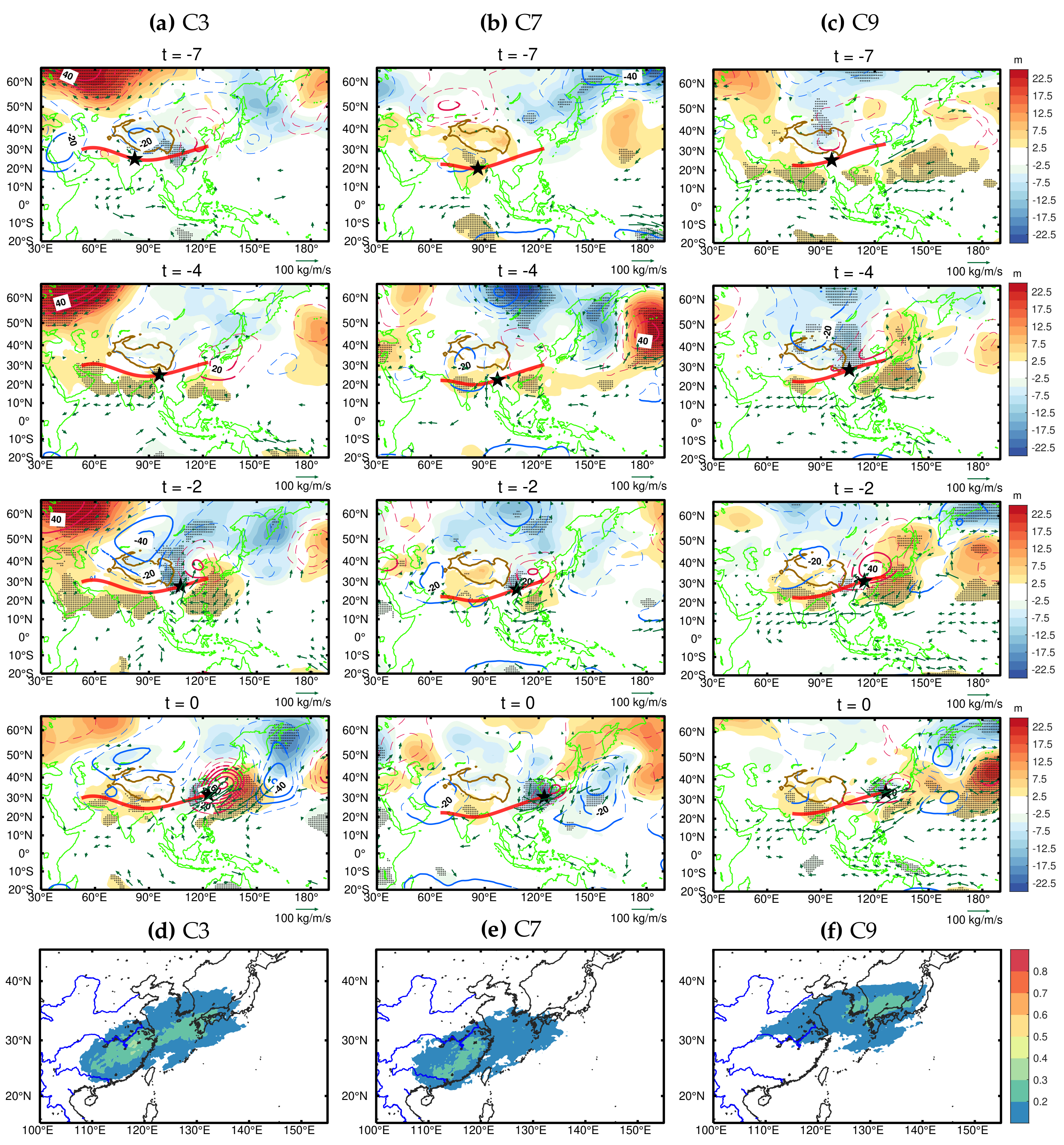

(a) C3
(b) C7
(c) C9
t = -7
t = -4
t = -2
t = 0
100 kg/m/s
m
(d) C3
(e) C7
(f) C9

Figure 4.

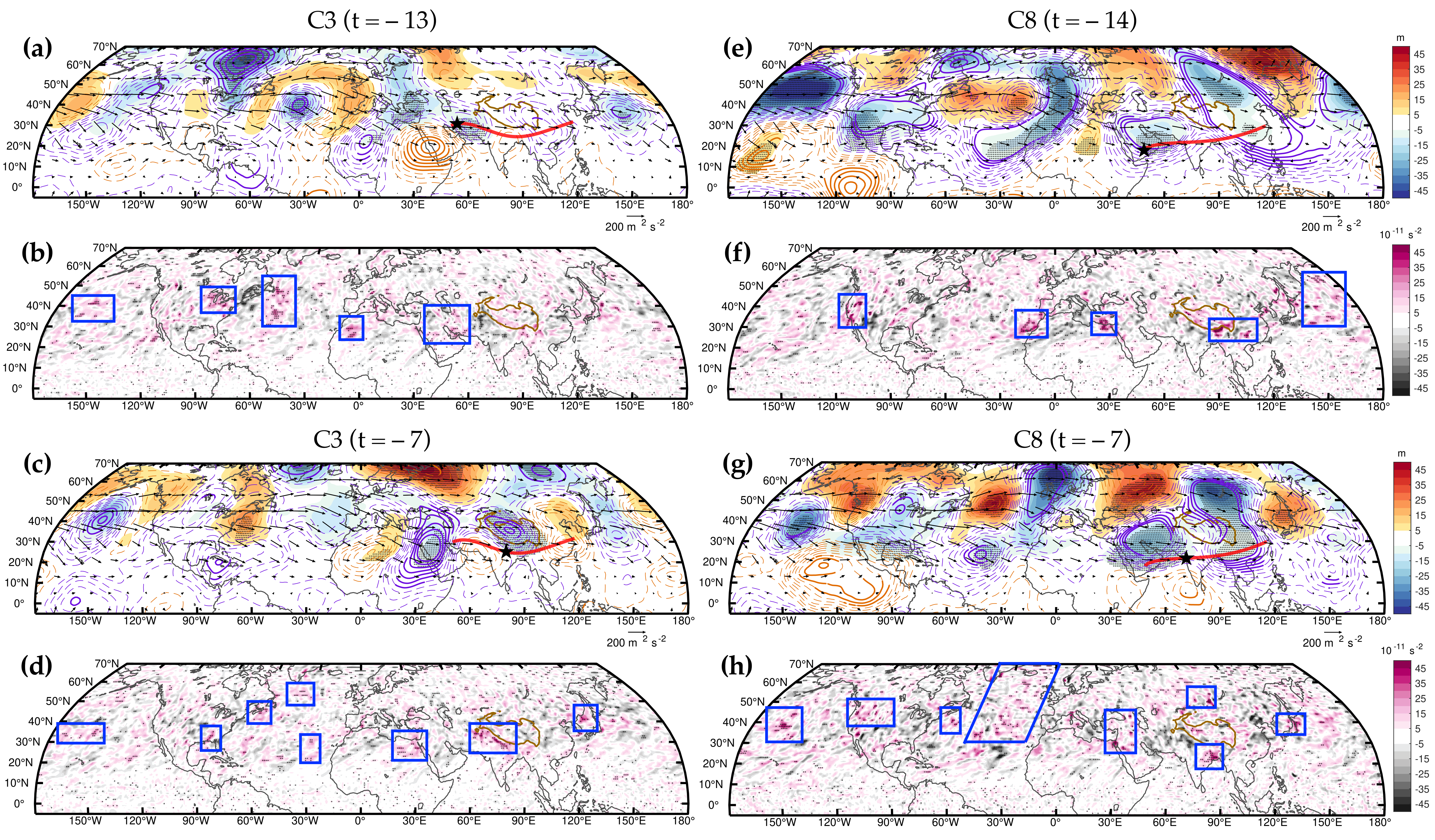
C3 (t = – 13)
C8 (t = – 14)
C3 (t = – 7)
C8 (t = – 7)
(a)
(b)
(c)
(d)
(e)
(f)
(g)
(h)
200 m 2 s -2
m
10 -11 s -2
70°N
60°N
50°N
40°N
30°N
20°N
10°N
0°
150°W
120°W
90°W
60°W
30°W
0°
30°E
60°E
90°E
120°E
150°E
180°
45
35
25
15
5
-5
-15
-25
-35
-45